Rare Metal Materials and Engineering
Volume 55, Issue 1, January 2026
Available online at www.rmme.ac.cn

Science Press

Cite this article as: Liu Junwei, Liu Zhenya, Fan Caihe, et al. Mechanical Anisotropy of Ti-6Al-4V Alloy Fabricated by Selective Laser Melting[J]. Rare Metal Materials and Engineering, 2026, 55(01): 35-46. DOI: https: //doi.org/10.12442/j.issn.1002-185X.20240819.

ARTICLE

Mechanical Anisotropy of Ti-6Al-4V Alloy Fabricated by Selective Laser Melting

Liu Junwei[1], Liu Zhenya[2], Fan Caihe[1], Ou Ling[1], He Wuqiang[1], Ma Wudan[1]

[1] School of Materials Science and Engineering, Hunan University of Technology, Zhuzhou 412007, China; [2] School of Material Science and Engineering, Nanchang Hangkong University, Nanchang 330063, China

Abstract: To explore the formation mechanism of anisotropy in Ti-6Al-4V alloy fabricated by selective laser melting (SLM), the compressive mechanical properties, microhardness, microstructure, and crystallographic orientation of the alloy across different planes were investigated. The anisotropy of SLM-fabricated Ti-6Al-4V alloys was analyzed, and the electron backscatter diffraction technique was used to investigate the influence of different grain types and orientations on the stress-strain distribution at various scales. Results reveal that in room-temperature compression tests at a strain rate of 10^{-3} s^{-1}, both the compressive yield strength and microhardness vary along the deposition direction, indicating a certain degree of mechanical property anisotropy. The alloy exhibits a columnar microstructure; along the deposition direction, the grains appear equiaxed, and they have internal hexagonal close-packed (hcp) α/α' martensitic structure. α' phase has a preferential orientation approximately along the <0001> direction. Anisotropy arises from the high aspect ratio of columnar grains, along with the weak texture of the microstructure and low symmetry of the hcp crystal structure.

Key words: selective laser melting; Ti-6Al-4V; anisotropy; crystal orientation

1 Introduction

Ti-6Al-4V has high specific strength, excellent fatigue strength, corrosion resistance, and biocompatibility, making it widely used in the medical and aerospace fields[1]. However, titanium and its alloys are relatively high-cost materials, and in conventional manufacturing processes, up to 80% of the raw materials are underutilized[2]. Selective laser melting (SLM), an additive manufacturing technology, can solve the problems of traditional manufacturing methods for titanium alloy components, including high costs, serious material waste, complex processes, and difficult post-processing[3]. Compared with that treated by conventional metal processing technology, the strength of titanium alloy parts prepared by SLM is comparable to that of forged counterparts[4]. Additionally, SLM provides unique advantages in realizing complex shape, enabling product customization and improving material utilization[5–6].

Extensive research has been conducted on the microstructure and mechanical properties of SLM-fabricated parts. Liu et al[7] found that the microstructure of SLM-fabricated Ti-6Al-4V alloy shows unique crystal structure characteristics: a checkerboard pattern in the *x*-*y* plane and coarse primitive β columnar grains in the *x*-*z* plane, accompanied by mechanical anisotropy. Li et al[8] found that the mechanical anisotropy of Ti-6Al-4V alloy formed by SLM was derived from the epitaxially grown β columnar grains and acicular martensitic α' phase in the as-deposited state. Although low-cycle fatigue performance was significantly improved by heat treatment through adjusting the microstructure, anisotropy still existed due to differences in crystal orientation. Zhu et al[9] studied the formation mechanism of SLM-fabricated Ti-6Al-4V parts, noting that their microstructure was shaped by complex thermal cycling during processing, including rapid solidification, directional heat dissipation, and repeated melting. Liu et al[10] found that

Received date: January 16, 2025
Foundation item: National Natural Science Foundation of China (51504138, 51674118, 52271177); Hunan Provincial Natural Science Foundation of China (2023JJ50181); Supported by State Key Laboratory of Materials Processing and Die & Mould Technology, Huazhong University of Science and Technology (P2024-022)
Corresponding author: Fan Caihe, Ph. D., Professor, School of Materials Science and Engineering, Hunan University of Technology, Zhuzhou 412007, P. R. China, Tel: 0086-731-22182188, E-mail: 369581813@qq.com

dislocations are also generated during martensitic transformation, leading to a high dislocation density. Grain boundaries, and residual stress can hinder the dislocation slip, resulting in high strength but poor plasticity in the alloy. Marco et al[11] found that the fully martensitic microstructure of SLM-fabricated Ti-6Al-4V contributes to its high strength yet low ductility. Since the martensitic crystal has a hexagonal close-packed (hcp) crystal structure, internal dislocation slip is inherently challenging[12–14]. Compared to face-centered cubic (fcc) and body-centered cubic (bcc) structures, the hcp structure is less symmetric[15]. Texture affects the strength, creep resistance, fatigue performance, and processability of materials, and it also has an important impact on the material anisotropy[16–17]. Soufiani et al[18] found that the SLM-fabricated Ti-6Al-4V alloy contains columnar prior β grains aligned along the processing direction, leading to greater plasticity along the growth direction than perpendicular direction. Vrancken et al[19] found texture in SLM-fabricated Ti-6Al-4V samples and speculated that texture is one of the reasons for the mechanical anisotropy. Niendorf et al[20] found that the SLM-fabricated 316L stainless steel exhibits texture. When the laser intensity is increased, the texture becomes more pronounced, finally forming a preferred structure. There is significant anisotropy in plasticity and strength, and the Young's modulus is also greatly reduced. Thijs et al[21] studied SLM-fabricated Ta and observed the formation of a strong texture. Compression tests showed that the yield strength in the horizontal direction is much lower than that in the vertical direction, due to the obvious vertical alignment of the columnar prior β grains, which hinders the {112} and {110} slip systems under vertical loading. Vialro et al[22] found that the mechanical properties of SLM-fabricated Ti-6Al-4V samples, especially ductility, exhibit anisotropy caused by defects in different directions. However, with the continuous progress of SLM technology, the defects of printed samples have been significantly reduced. But the mechanical anisotropy of SLM-fabricated Ti-6Al-4V alloy still exists.

Based on the above analysis, there remains a lack of studies on how microstructural anisotropies and crystallographic preferred orientations of SLM-fabricated Ti-6Al-4V alloy induce mechanical property anisotropy. Addressing this research gap, the compressive properties and microhardness of SLM-fabricated Ti-6Al-4V alloys across different planes were analyzed comparatively. Then, the microstructure and crystallographic orientation were analyzed through electron backscatter diffraction (EBSD) analysis and other characterization techniques. These efforts aim to establish the relationship among mechanical properties, microstructure, and crystallographic orientation, explore the causes of anisotropy, and ultimately lay the groundwork for weakening and eliminating anisotropy in SLM-fabricated Ti-6Al-4V alloy.

2 Experiment

The Ti-6Al-4V powder used in this experiment was prepared by electrode induction gas atomization (EIGA). As shown in Fig.1, a powder particle size range of 15–56 μm was selected for SLM processing. The particle size distribution of the powder was characterized using an LS-POP(9) laser particle size analyzer, and its chemical composition is shown in Table 1. Before SLM, the Ti-6Al-4V powder was placed in a vacuum drying oven, heated to 150 ℃, held for 4 h, and then cooled to room temperature before being removed.

The experiment was conducted using a EOS M290 SLM system from Germany. During the experiment, high-purity argon (99.9%) was introduced as the protective gas to prevent oxidation. A stripe scanning strategy was employed with a 5 mm scanning pitch. The specific SLM processing parameters are as follows: powder laying thickness of 60 μm, laser power of 150 W, scanning speed of 1250 mm/s, and laser spot diameter of 100 μm. Both horizontal and vertical samples were prepared with an offset of 1 mm. The substrate used in this work was Ti-6Al-4V plate with dimensions of 250 mm× 250 mm×20 mm. As shown in Fig. 2, to better evaluate the mechanical anisotropy of SLM-fabricated Ti-6Al-4V alloy, the samples were defined as follows. Horizontal samples are oriented parallel to the construction direction, with dimensions of 13 mm×13 mm×75 mm, and vertical samples are oriented perpendicular to the substrate, with dimensions of Φ13 mm×75 mm.

The compressive mechanical properties of the samples were tested using a WDW-E100D microcomputer-controlled electronic universal testing machine. Room-temperature compression tests were conducted at strain rates of 10^{-3} and 10^{-4} s^{-1}; cylindrical samples with dimensions of Φ4 mm×6 mm were used for the tests, and the compressive properties were subsequently analyzed. To better evaluate the mechanical anisotropy, the samples were subjected to external loading in the vertical directions of the *XOY* plane and the *YOZ* plane.

Microhardness testing of the SLM-fabricated Ti-6Al-4V alloy samples was performed using an HR-150A Vickers hardness tester. For each sample, 9 test points were selected, with an interval of 200 μm between adjacent points. The

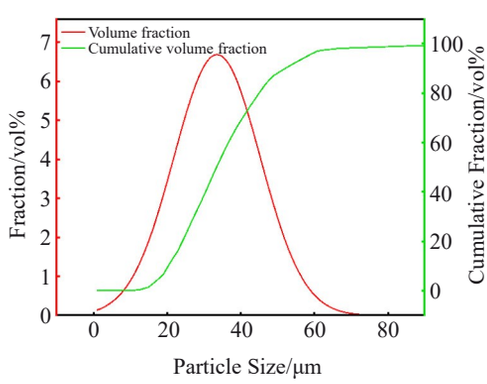

Fig.1 Particle size distribution of Ti-6Al-4V alloy powder

Table 1 Chemical composition of Ti-6Al-4V powder (wt%)

Al	V	Fe	C	O	N	Ti
6.16	4.10	0.30	0.12	0.39	0.03	Bal.

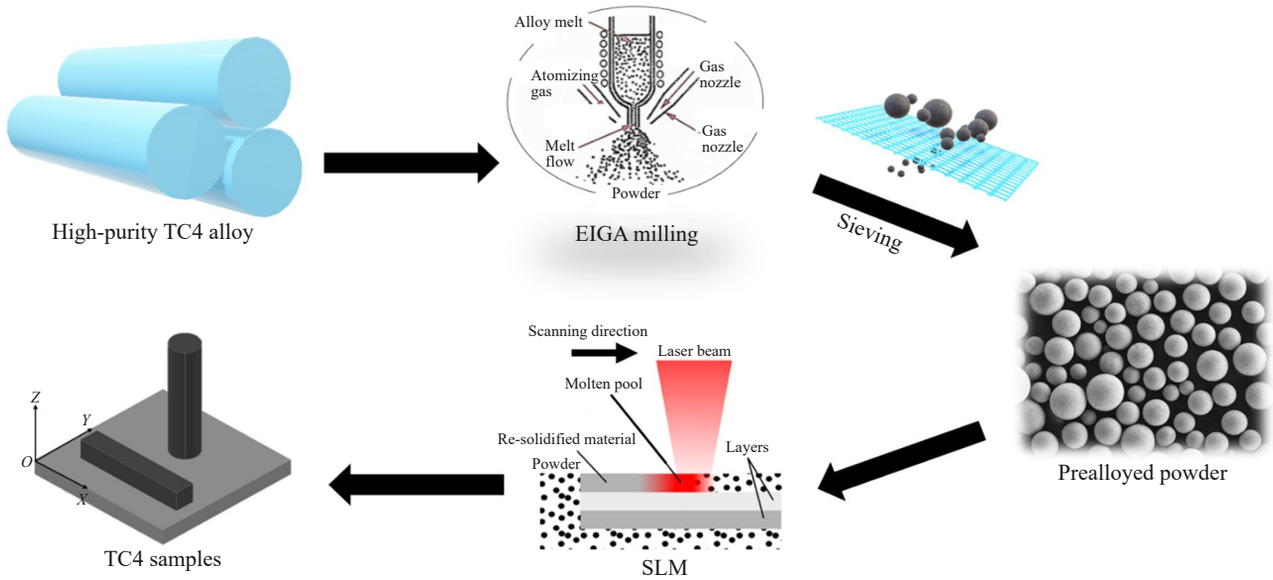

Fig.2 Process flow diagram for SLM-fabricated Ti-6Al-4V samples

loading force was 200 g, and the loading time was 20 s. The average microhardness value of the 9 points was calculated and used as the final microhardness result for the sample.

To characterize the phase composition of the SLM-fabricated Ti-6Al-4V alloy, X-ray diffractometer (XRD, D8 ADVANCE-A25, produced by Bruker, Germany) was employed, and the phase composition was analyzed using Jade software.

Metallographic samples of SLM-fabricated Ti-6Al-4V alloy were prepared via standard mechanical polishing. Subsequently, the polished samples were etched using Kroll's reagent with a volume ratio of HF: HNO_3: H_2O=2: 1: 17. The etching process was conducted via the wiping method, with a controlled etching time of 25 s. The microstructure of the transverse and longitudinal sections of the samples was observed using an XJP-6A optical microscope (OM) and a FEI Nova Nano SEM450 field emission scanning electron microscope (SEM). The macroscopic morphology of the samples was observed using a metallographic microscope, while their microstructures were examined with SEM. The samples were polished with argon ions, and EBSD was performed with a step size of 0.4 μm. EBSD measurement was performed using a JSM-7800F field emission SEM equipped with a NordlysMax3 EBSD detection system. This setup enables high-precision mapping of crystallographic orientations.

3 Results and Discussion

3.1 Compressive mechanical properties

Fig. 3a shows the compressive stress-compressive strain curves of SLM-fabricated Ti-6Al-4V alloy tested at a strain rate of 10^{-3} s^{-1}. For the *YOZ* plane (parallel to the deposition direction), the compressive yield strength (CYS) is 1628 MPa, with a corresponding compressive strength (CS) of 1980 MPa and a failure strain of 16.9%. Conversely, for the *XOY* plane

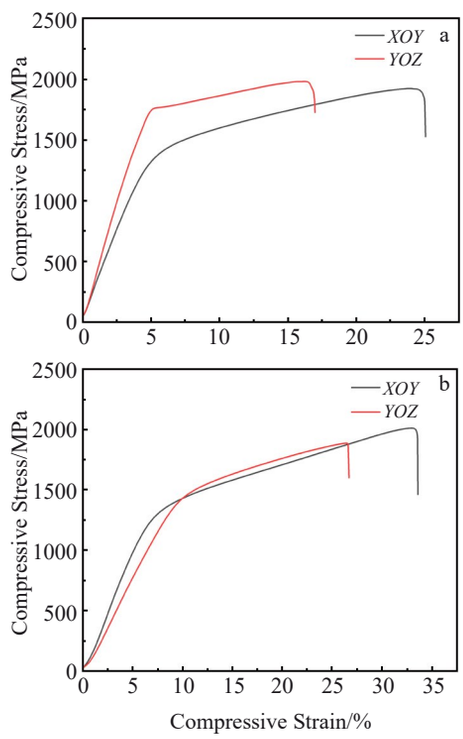

Fig.3 Compressive stress-compressive strain curves of SLM-fabricated Ti-6Al-4V alloy compressed horizontally and vertically at different strain rates: (a) 10^{-3} s^{-1} and (b) 10^{-4} s^{-1}

(perpendicular to the deposition direction), the CYS is 1423 MPa, with a corresponding CS of 1923 MPa and a failure strain of 25.1%. Notably, there is a pronounced disparity in mechanical properties between the two planes, confirming the presence of mechanical anisotropy. Owing to the high temperature gradient and rapid cooling rate in the SLM process, the sample exhibits a large volume fraction of needle-like α' phases. As a result, the CS of SLM-fabricated

alloy exceeds that of traditionally cast and forged Ti-6Al-4V alloys. However, these needle-like α' phases act as barriers to dislocation slip, restricting the slip distance of dislocations during compression, causing a significant reduction in plasticity of alloy.

The difference ratio of compressive properties between horizontal and vertical samples is defined as follows[23]:

$$\eta = 2\left|\frac{P_{\text{horizontal}} - P_{\text{vertical}}}{P_{\text{horizontal}} + P_{\text{vertical}}}\right| \times 100\% \quad (1)$$

where η is the difference ratio of compressive properties; $P_{\text{horizontal}}$ and P_{vertical} are the compressive property parameters of the horizontal and vertical samples, respectively. The difference ratio of CYS is 12.6%, the difference ratio of ultimate compressive strength is 2.8%, and the difference ratio of failure strain is 31.9%. This significant variation in anisotropy across different properties may be related to the distinct microstructural morphologies in the cross-sections of the horizontal and vertical samples.

Fig. 3b shows the compressive stress-compressive strain curve of the alloy tested at a strain rate of 10^{-4} s^{-1}. It is observed that at room temperature, the lower the strain rate, the greater the peak strain. The CYS of the horizontal samples is 1113 MPa, with a corresponding failure strain of 28.8%; in comparison, for vertical samples, the yield strength is 1366 MPa and the corresponding failure strain is 33.5%. The difference ratio of yield strength and compressive strength between the two orientations is calculated to be 18.52% and 6.21%, respectively.

3.2 Microhardness

Table 2 presents the microhardness values of the SLM-fabricated Ti-6Al-4V alloy in the *XOY*, *XOZ*, and *YOZ* planes. It is observed that the microhardness values on the *XOY* plane (perpendicular to the deposition direction) are all above 430 $HV_{0.2}$, while the average microhardness values on the *XOZ* and *YOZ* planes (parallel to the deposition direction) are 413 and 415 $HV_{0.2}$, respectively. In other words, the average microhardness perpendicular to the deposition direction is 414 $HV_{0.2}$. Owing to the high relative density of SLM-fabricated samples and the direct influence of relative density on microhardness, the microhardness of SLM-fabricated Ti-6Al-4V alloy (ranging from 375 $HV_{0.2}$ to 480 $HV_{0.2}$) surpasses that of conventionally forged Ti-6Al-4V alloy (ranging from 380 $HV_{0.2}$ to 430 $HV_{0.2}$)[24].

Table 2 Microhardness values of different planes of SLM-fabricated Ti-6Al-4V alloy ($HV_{0.2}$)

Sample	*XOY*	*XOZ*	*YOZ*
1	434	414	419
2	432	413	408
3	430	415	416
4	436	412	412
5	434	415	418
6	440	408	415
7	440	414	419
8	430	410	415
9	439	416	413

As depicted in Fig.4, the average microhardness of the *XOY* plane is 435 $HV_{0.2}$, whereas that of the *XOZ* and *YOZ* planes are 413 and 415 $HV_{0.2}$, respectively. While relative density can influence material hardness, previous studies have indicated that when the relative density is sufficiently high, the microstructural features of material become the significant factor determining hardness[25]. During the SLM process, ultra-fine α' martensite forms, enhancing the microhardness of the Ti-6Al-4V alloy. The microhardness of the SLM-fabricated Ti-6Al-4V alloy increases with decreasing the width and spacing of α' martensitic laths[26].

3.3 XRD analysis

Fig. 5 presents the XRD patterns of the SLM-fabricated Ti-6Al-4V alloy sample, revealing characteristic diffraction peaks corresponding to the α/α'-Ti phase with a hcp structure. Upon calculation, the lattice parameters for the *XOY*, *XOZ*, and *YOZ* planes are as follows: a_{XOY}=0.2936 nm, c_{XOY}=0.4667 nm, a_{XOZ}=0.2924 nm, c_{XOZ}=0.4678 nm, a_{YOZ}=0.2929 nm, and c_{YOZ}=0.4668 nm. These lattice parameters are comparable to the reported values of the α' phase (a=0.2931 nm; c=0.4681 nm)[27].

The SLM-fabricated Ti-6Al-4V alloy experiences an rapid cooling rate that significantly exceeds the critical cooling rate required for martensitic transformation (410 K/s)[28], resulting

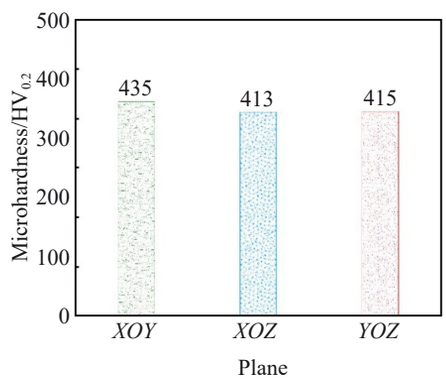

Fig.4 Microhardness of different planes of SLM-fabricated Ti-6Al-4V alloy

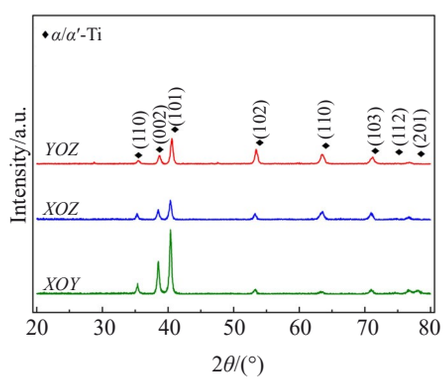

Fig.5 XRD patterns of SLM-fabricated Ti-6Al-4V alloy

in the formation of the α' phase in the SLM-fabricated Ti-6Al-4V alloy. Although the α' phase exhibits greater strength and hardness compared to both α and β phases, it exhibits inferior plasticity[29]. This accounts for the inferior plasticity of the SLM-fabricated Ti-6Al-4V alloy. Additionally, during the SLM process, heat dissipation primarily occurs along the negative *Z*-axis direction, and its distribution varies across different planes within the same sample, ultimately resulting in preferentially oriented martensite and thereby inducing anisotropy.

3.4 Microscopic morphology

Fig.6 depicts the metallographic microstructure of the SLM-fabricated Ti-6Al-4V alloy. No evident laser scanning traces are observed, and the boundaries between adjacent grains exhibit a microstructure approximately perpendicular to the substrate, which consists of the columnar prior β grains. These columnar grains grow outward in the heat dissipation direction, with lengths reaching the millimeter scale and penetrating multiple powder layers. The interior of the columnar β grains is characterized by needle-shaped α' phases. From a macroscopic perspective, no noticeable defects, such as pores or cracks, are detected in the alloy, indicating a high relative density of 99.61%. The microstructures of the cross-sections of both vertical and horizontal samples exhibit distinct morphologies, consistent with findings from Ref.[23,30].

Fig.6a shows an equiaxed morphology on the *XOY* plane of the horizontal sample, whereas Fig.6c and 6e depict columnar grain structures on the *XOZ* and *YOZ* planes of horizontal sample, respectively. This microstructural difference arises from the directional growth behavior of grains during SLM: columnar grains tend to grow along the direction perpendicular to the thermal conduction direction of substrate with significant temperature gradient variations. The columnar grains extend upward along the printing direction with lengths exceeding several hundred micrometers (far greater than the powder layer thickness) and widths ranging from tens to hundreds of micrometers. As a result, the *XOY* plane (parallel to the substrate) displays a clear equiaxed structure, while the *XOZ* and *YOZ* planes (perpendicular to the substrate) exhibit distinct columnar morphologies.

The microhardness of the *XOY* planes is relatively high, which is due to the presence of many elongated and short needle-like α' phases within the equiaxed grains, while the columnar grains extend up to several hundred micrometers in length. Although needle-like structures also exist within the α' phase, their internal α' martensitic needles are significantly longer. Compared to the *XOZ* and *YOZ* planes, the *XOY* plane has a much higher grain boundary density. Due to the hindering effect of grain boundaries on dislocation motion and slip, the microhardness of the *XOY* plane is higher, resulting in a certain degree of microhardness anisotropy.

During the SLM fabrication of Ti-6Al-4V alloy, the combined effects of a high temperature gradient and the very fast cooling rate drive the martensitic phase transformation from β phase to α phase. Microstructural observations reveal distinct differences across planes. As in Fig.6b, the *XOY* planes exhibit a clear equiaxial grain morphology with needle-like α' phases distributed inside the grains. As shown in Fig. 6d and 6f, the columnar grains observed from the *XOZ* and *YOZ* planes are composed of acicular α' phases, which are staggered at an angle of 60° and arranged in bundles. These acicular α' bundles have a high aspect ratio with widths generally less than 1 μm. However, the acicular α' phase inside the columnar grains is longer, and that inside the equiaxed grains is finer, confirming that there is microstructural anisotropy in the SLM-fabricated alloy. Such microstructural anisotropy, particularly variations in the number and orientation of grain boundaries across different planes, is presumably responsible for the directional differences in mechanical properties.

Fig. 7 shows SEM images of the microstructure of SLM-fabricated Ti-6Al-4V alloy. As shown in Fig. 7a, the *XOY*

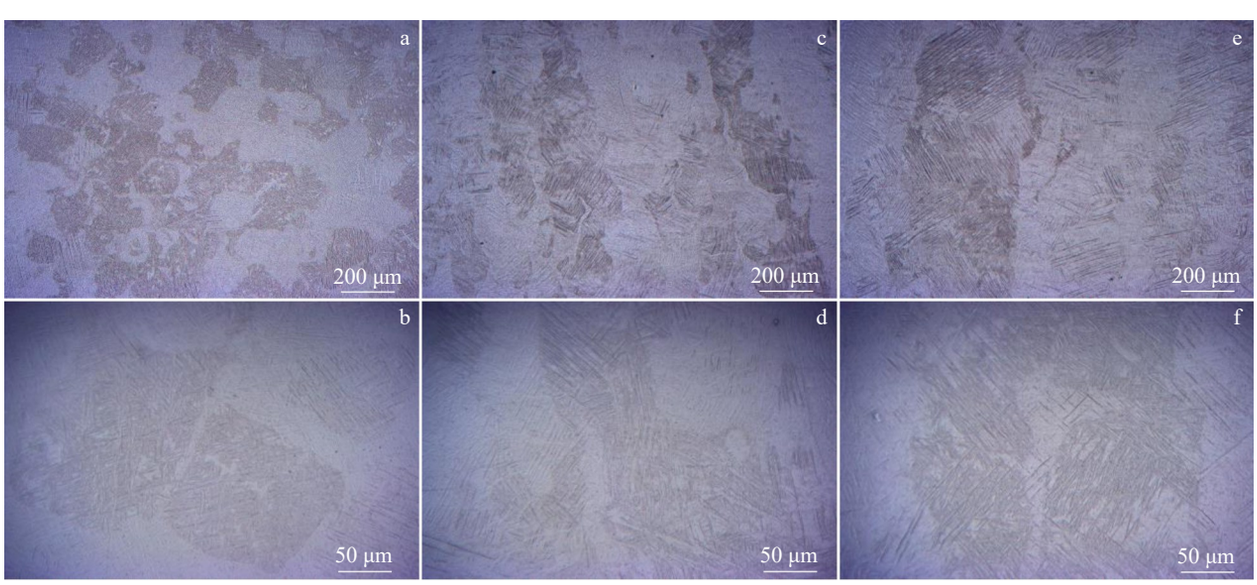

Fig.6 Macroscopic morphologies of different planes of SLM-fabricated Ti-6Al-4V alloy: (a–b) *XOY* planes, (c–d) *XOZ* planes, and (e–f) *YOZ* planes

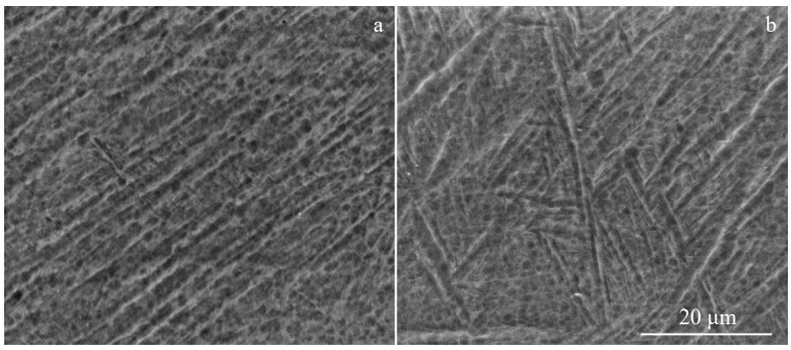

Fig.7 SEM morphologies of SLM-fabricated Ti-6Al-4V alloy along *XOY* plane (a) and *YOZ* plane (b)

planes have obviously oriented needle-like α phase, which is due to the columnar phase and high aspect ratio, presenting a characteristic of 60° crystallographic orientation. As shown in Fig. 7b, many fine acicular α phases are observed in the *YOZ* plane, which are internally interlaced, forming a typical basket-weave microstructure.

Due to the extremely high temperature gradient (up to 10^6 K/m) during the SLM process, columnar prior β grains and preferentially oriented acicular α' phases are formed through the following mechanism. When the laser is irradiated on the Ti-6Al-4V powder bed, the local temperature rapidly exceeds the β-transus temperature, inducing martensitic transformation. Due to the rapid cooling rate, the bcc β phase is transformed directly into hcp one, resulting in nearly complete conversion of the β phase to needle-like α' phases. The α' martensite phases exhibit significant size variation: the longest martensite laths exceed 100 μm in length with a width of 1–2 μm, while the smallest ones are only a few hundred nanometers in length. This size heterogeneity is due to the repetitive heating and cooling cycles during the SLM process, leading to the formation of the aforementioned diverse martensite structures.

The fracture morphologies of the SLM-fabricated Ti-6Al-4V alloy are shown in Fig. 8. Specifically, Fig. 8a reveals numerous cleavage steps, which arise from dislocation slip during compressive loading. In Fig. 8b, a large number of large and smooth facets alongside small-scale parabolic ligament-like dimples are observed. Notably, no ligament-like dimples are found within the second phase regions, further confirming the brittle fracture. As shown in Fig. 8c, vertical samples contain more ligament-like dimples compared to horizontal samples (Fig. 8d), and the dimples in vertical samples are also larger in size. Generally, larger ligament-like dimples correspond to better plastic deformation capacity, indicating that vertical samples possess superior plasticity than horizontal samples.

3.5 EBSD analysis

In order to observe the grain orientation and morphology of Ti-6Al-4V alloy formed by SLM, the *XOY* and *YOZ* planes of the horizontal samples were analyzed using EBSD.

As shown in Fig. 9, different cross-sections exhibit intert-

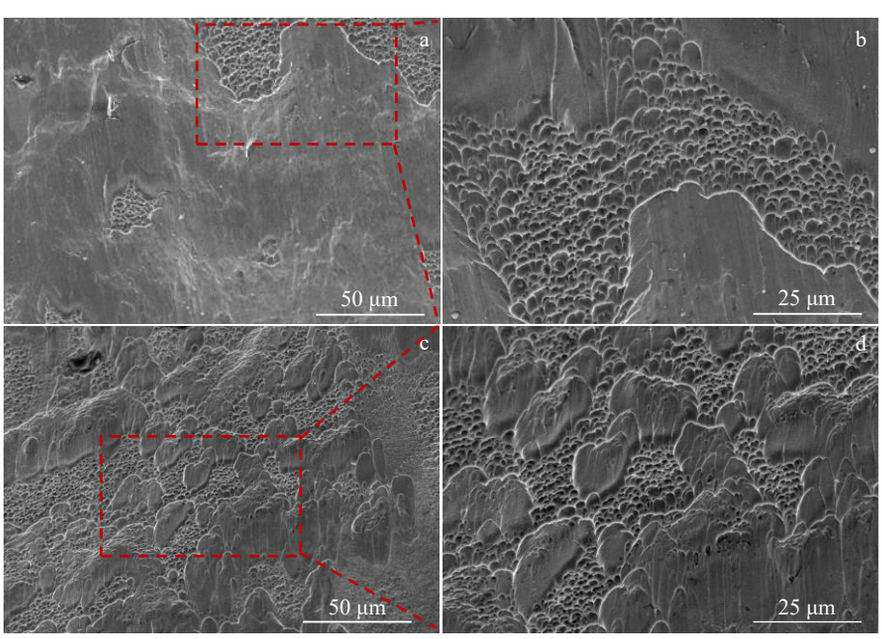

Fig.8 Fracture morphologies of SLM-fabricated Ti-6Al-4V alloy along horizontal direction (a–b) and vertical direction (c–d)

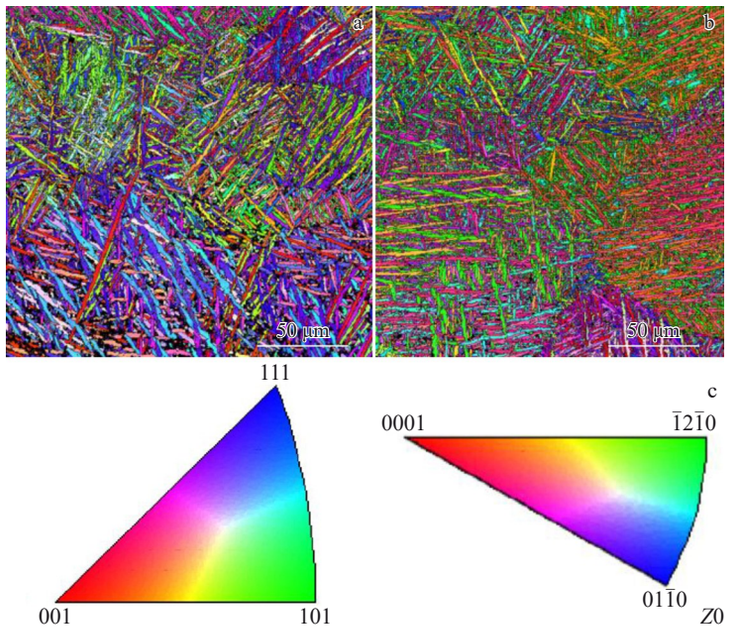

Fig.9 EBSD maps and grain orientation distributions of SLM-fabricated Ti-6Al-4V alloy along *YOZ* plane (a) and *XOY* plane (b); corresponding inverse pole figures (c)

wined fine acicular structures with grains displaying preferred orientations. These preferred orientations correspond to specific crystallographic directions, and the corresponding relationship is illustrated in Fig. 9c. The SLM-fabricated Ti-6Al-4V alloy forms needle-like α' phases with random orientations; these α' phases interweave to form a basketweave microstructure, while the parent grains still show overall preferential orientation. As shown in Fig.9a, within the prior β grains, the number of red oriented grains is significantly larger than that of green and blue oriented grains. Different directions correspond to distinct crystallographic orientations, and the corresponding relationship is illustrated in Fig. 9c. This indicates that the acicular α' phases in the SLM-fabricated Ti-6Al-4V alloy are mainly oriented along the <0001> direction with additional minor orientations including $<\bar{1}\,2\,\bar{1}\,0>$ and $<01\,\bar{1}\,0>$.

The same preferential orientation is also observed in the pole figures of the SLM-fabricated Ti-6Al-4V alloy (Fig. 10). Specifically, the pole figures reveal that the projected distribution of crystalline planes in the macroscopic coordinate system is more dispersed, indicating a weaker texture. Under the ultra-rapid cooling of SLM, the high-temperature β phase

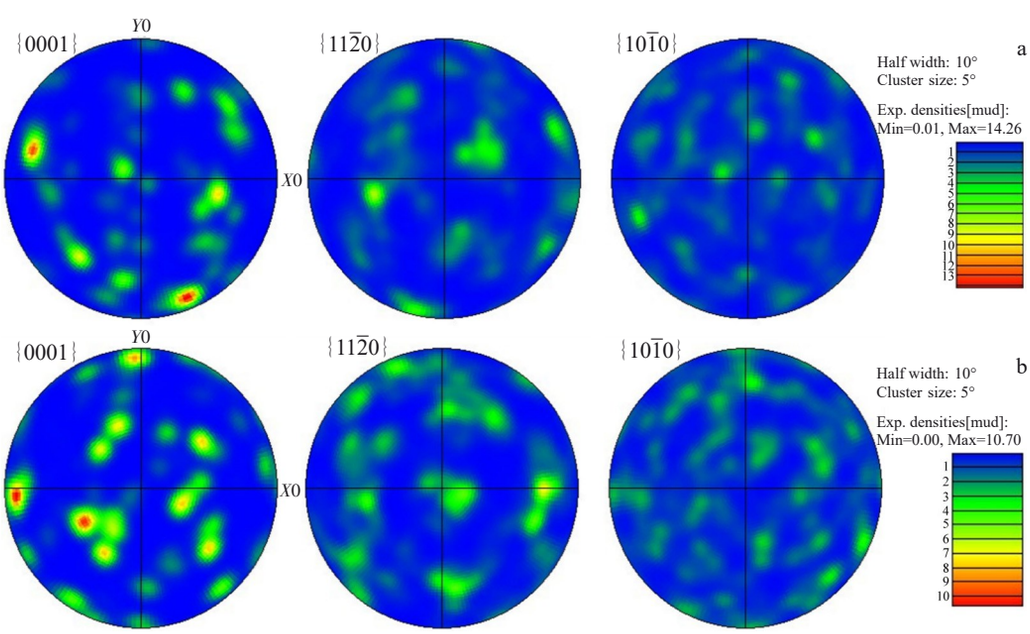

Fig.10 Pole figures of SLM-fabricated Ti-6Al-4V alloy along *YOZ* plane (a) and *XOY* plane (b)

is transformed into the α phase conforming to the Burgers orientation relation: $\{110\}_{\beta}//\{0001\}_{\alpha'}$ and $<1\bar{1}1>_{\beta}//<11\bar{2}0>_{\alpha'}$. Since the single-orientation β phase has 2 independent slip directions and 6 possible slip planes, it can be transformed into 12 distinct orientations of α/α' phases[19]. The texture intensity along <0001> direction in the *YOZ* plane is measured as 14.26, while it in the *XOY* plane is 10.07. There is epitaxial growth of columnar prior β grains in the *YOZ* plane, leading to greater texture intensity and more pronounced selective crystallographic orientation.

Fig. 11 presents the phase distribution maps of SLM-fabricated Ti-6Al-4V alloy, where the color coding is defined as follows: white represents the α phase, green represents the β phase, and black denotes the grain boundary of α phase. The results show that the α phase accounts for a dominant proportion of the microstructure, while the β phase only accounts for a small fraction. Most of the retained β phase is distributed at the grain boundaries of the α phase, which is due to the extreme temperature gradient and ultra-rapid cooling rate inherent to the SLM process. Therefore, most of the β phase is converted into α phase during the cooling process, but a small amount of the β phase fails to undergo complete transformation and is retained at the grain boundaries of the α phase.

Fig. 12a and 12b show the orientation difference distributions between α-Ti and β-Ti phases of the *YOZ* plane, Fig. 12c and 12d show corresponding orientation difference distributions of the *XOY* plane. These orientation differences reflect the rotational relationships between grains of the same phase. As shown in Fig. 12, on the *YOZ* and *XOY* planes, the main orientation differences of the α' phases are the same, roughly distributed in three ranges: 0°–5°, 55°–65°, and 85° – 90°. These orientation difference characteristics correspond to the staggered distribution of martensite laths in Fig. 9b. The orientation difference distribution of the β phase is mainly focused on three other ranges: 0°–3°, 27°–33°, and 57°–60°.

The *XOY* plane contains more small-angle grain boundaries of the β phase than the *YOZ* plane. This is presumably attributed to the cooling rate difference between the two planes: the *XOY* plane (parallel to the substrate) experiences a relatively high cooling rate during SLM, leaving the β phase with insufficient time for grain growth. Consequently, a greater number of fine-grained β phases are formed, thereby increasing the density of small-angle grain boundaries. In the Ti-6Al-4V alloy, the $\beta \rightarrow \alpha$ phase transformation follows the Burgers orientation relationship, and the misorientation angles of 10.5° , 60.0° – 63.3° , and 90.0° arise from inherent crystallographic constraints and variant selection during transformation[31]. For the α phase on the *XOY* plane, the proportion of small-angle grain boundaries in the 0° – 5° misorientation range is 30.68%, and the proportion of large-angle grain boundaries in the vicinity of 60° is 48.78%. For the β phase on the same plane, the proportion of small-angle grain boundaries in the misorientation range of 0°–10° is 24%. The proportion of large-angle grain boundaries near 30° is 52%, and that near 60° is 24%. In *YOZ* planes, for the α phase, the proportion of small-angle grain boundaries in the range of 0° – 5° is 27.46%, and the proportion of large-angle grain boundaries near 60° is 57.81%; for the β phase, the proportion of small-angle grain boundaries in the range of 0° – 10° is 48.4%, the proportion of large-angle grain boundaries near 30° is 33.9%, and that near 60° is 16.1%. Thus, it can be shown that the α phase with an orientation difference angle of 60° is produced by the $\beta \rightarrow \alpha$ phase transformation.

Fig. 13 shows the distribution of grain types in the *YOZ* plane of SLM-fabricated Ti-6Al-4V alloy. Based on size and formation sequence, the α' martensite can be categorized into primary, secondary, and tertiary α martensite[32]. As shown in Fig. 13a_1, primary α' martensite has a length of up to 10 μm or longer and a width of a few micrometers. The primary martensite forms during the SLM process and has a large grain area. As shown in Fig. 13a_3, the aspect ratios of primary martensite are mainly concentrated in the range of 1–10 with the highest frequency observed at an aspect ratio of 3. In contrast, secondary and tertiary α' martensites are generated during the solidification and cooling stages of the alloy. The grain area is substantially reduced, primarily because the secondary martensite is impeded by the primary martensite boundaries during the growth process. As shown in Fig. 13b_2 and 13b_3, secondary martensite has a length of several micrometers and a narrower width than the primary martensite; it grows either perpendicular or parallel to the

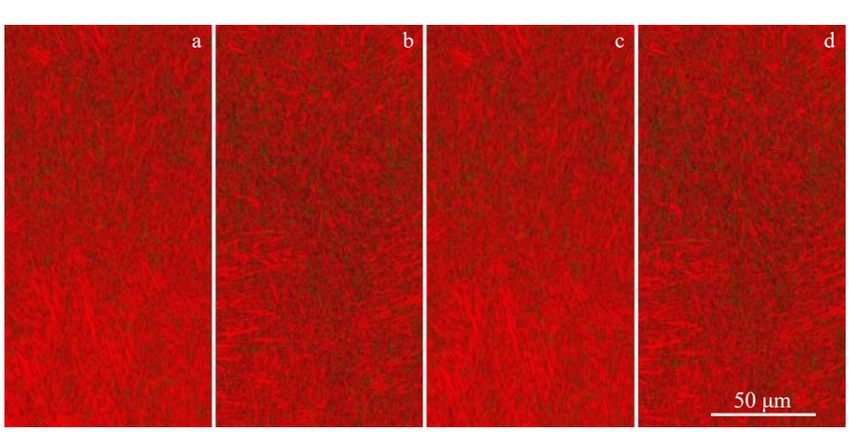

Fig.11 Phase distributions of SLM-fabricated Ti-6Al-4V alloy along *YOZ* plane (a–b) and *XOY* plane (c–d)

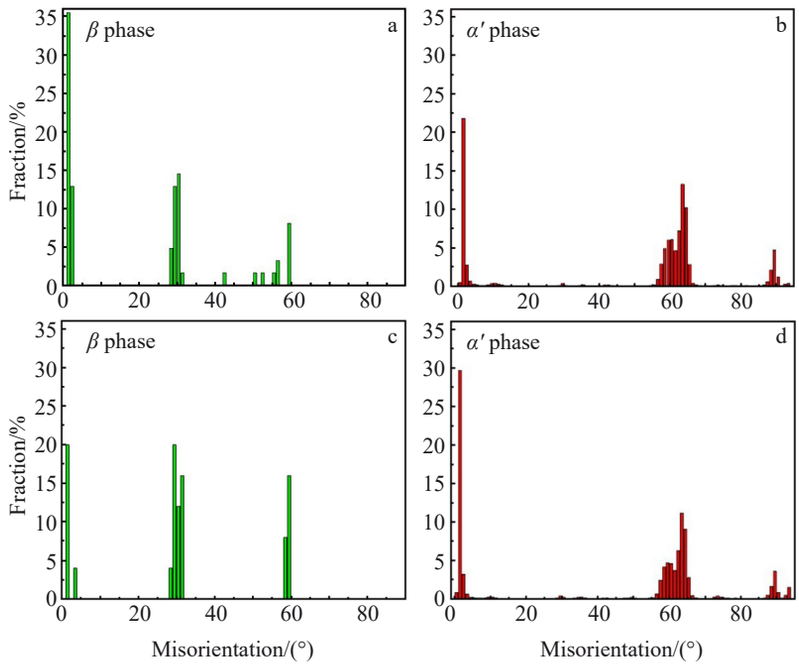

Fig. 12 Misorientation distribution of β phase (a, c) and α' phase (b, d) in *YOZ* (a–b) and *XOY* (c–d) planes of SLM-fabricated Ti-6Al-4V alloy

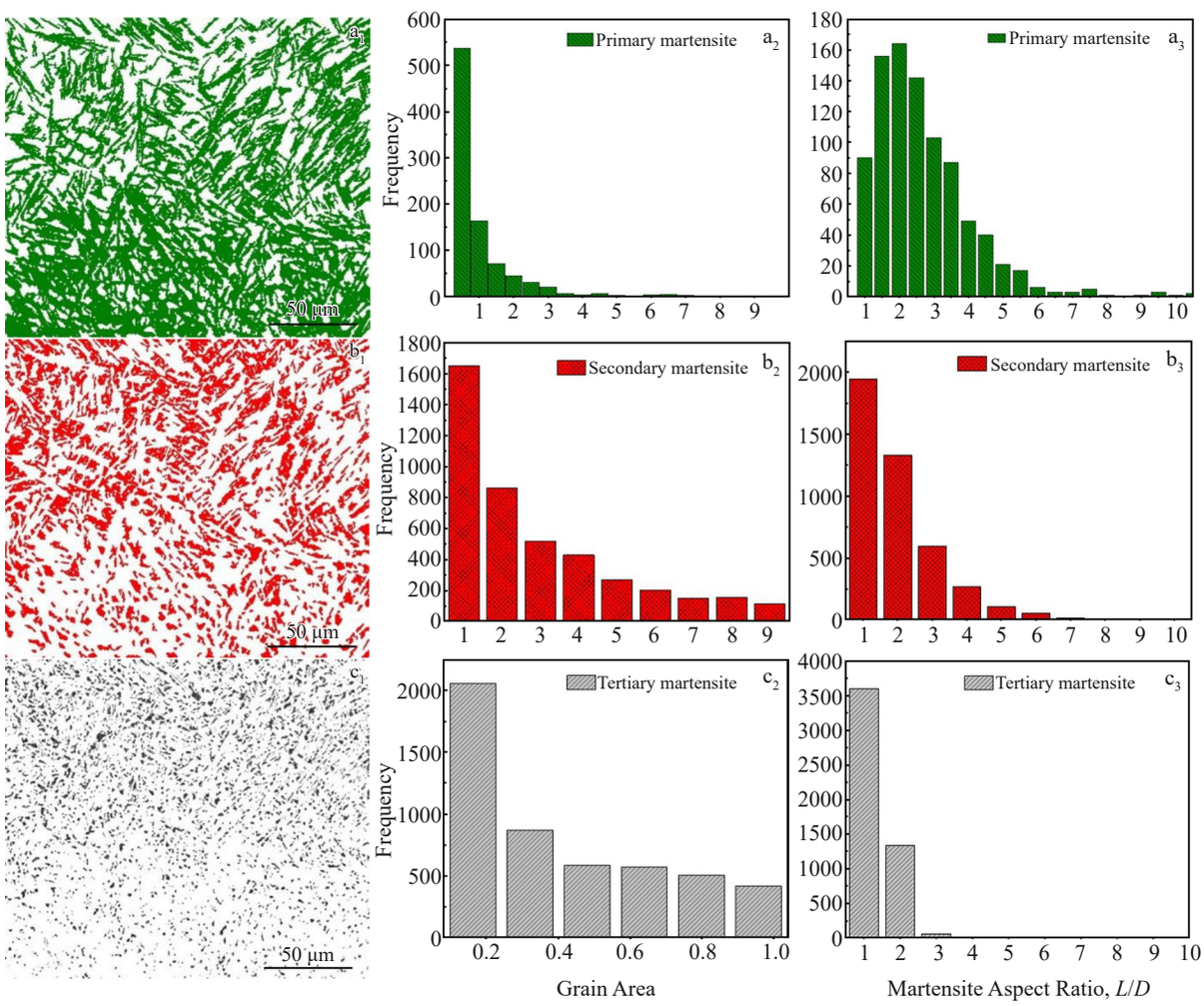

Fig. 13 Distribution of grains (a_1–c_1), grain area (a_2–c_2), and martensite aspect ratio (a_3–c_3) in *YOZ* plane of SLM-fabricated Ti-6Al-4V alloy: (a_1–a_3) primary martensite, (b_1–b_3) secondary martensite; (c_1–c_3) tertiary martensite

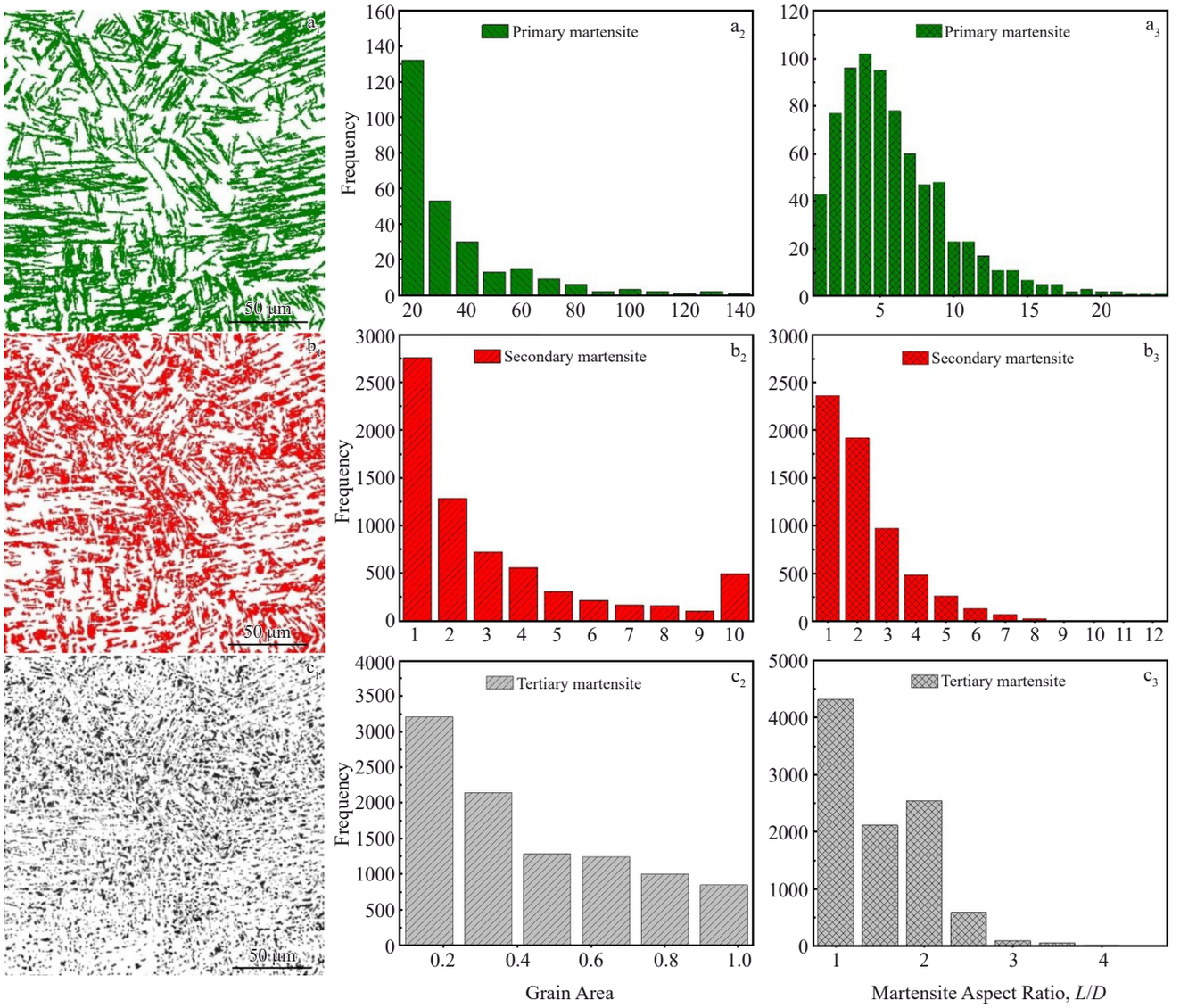

Fig.14 Distribution of grains (a_1–c_1), grain area (a_2–c_2), and martensite aspect ratio (a_3–c_3) in the *XOY* plane of SLM-fabricated Ti-6Al-4V alloy: (a_1–a_3) primary martensite, (b_1–b_3) secondary martensite; (c_1–c_3) tertiary martensite

primary martensite. The length-to-diameter (*L*/*D*) ratios of secondary martensite are mainly distributed in the range of 1 – 6 with the highest frequency at an *L*/*D* ratio of 1. The tertiary *α*′ martensite is similar to the secondary martensite, it also forms in the cooling and solidification stages, but has an even smaller grain area.

As shown in Fig. 13c_1 – 13c_3, the tertiary martensite has a length of less than 1 μm and a width of less than 100 μm. Its *L*/*D* ratios are mainly concentrated in the range of 1 – 3 with the highest frequency at an *L*/*D* ratio of 1. In summary, primary martensite is needle-like and has a relatively high *L*/*D* ratio, while the secondary and tertiary martensites are needle-like and equiaxed with a generally lower *L*/*D* ratio.

As shown in Fig. 14, the amount of primary martensite in the *XOY* plane is less than that in the *YOZ* plane, and the amount of secondary and tertiary martensites in the *XOY* plane is more. As shown in Fig. 14a_1 – 14a_3, the primary martensites has large size with a maximum grain area of 140.96 μm^2; its *L*/*D* ratios are mainly distributed in the range of 1 – 15, and the highest frequency occurs at an *L*/*D* ratio of 4. In contrast, the secondary and tertiary martensites have lower *L*/*D* ratios with the highest frequency concentrated at an *L*/*D* ratio of 1. Overall, the martensite in the *XOY* plane has a smaller grain area but a generally larger *L*/*D* ratio than that in the *YOZ* plane. Specifically, compared to the *YOZ* plane, the martensite in the *XOY* plane is shorter in length but higher in *L*/*D* ratio, which is one of the key factors contributing to the mechanical anisotropy of SLM-fabricated Ti-6Al-4V alloys.

4 Conclusions

1) For SLM-fabricated Ti-6Al-4V alloy, compression tests at room-temperature were performed at a strain rate of 10^{-3} s^{-1}. The yield strength and compressive fracture strength of the horizontal sample are higher than those of the vertical sample.

Specifically, the anisotropy degree of CYS is 12.6%, while that of the compressive failure strength is 2.8%. The failure strain shows an opposite trend to strength. The horizontal samples fracture at a compressive strain of 16.2%, whereas the vertical samples fracture at a compressive strain of 23.8%. The average microhardness parallel to the deposition direction is 439 $HV_{0.2}$, and the average microhardness perpendicular to the deposition direction is 414 $HV_{0.2}$. The mechanical properties and microhardness show a certain degree of anisotropy.

2) The microstructure of SLM-fabricated Ti-6Al-4V alloy consists of columnar prior β grains. Along the deposition direction, the grains exhibit a typical columnar morphology; along the deposition direction, the grains appear equiaxed under microscopical observation. All these grains compose internal hcp α/α' martensitic structure. These martensites exhibit a high aspect ratio, and the hcp crystallographic texture is weak with low symmetry, which collectively rises the anisotropy.

3) In the SLM-fabricated Ti-6Al-4V alloy, the α' phase exhibits a preferred orientation along the {0001} plane. These α' phases form staggered structures during repeated heating and cooling cycles, exhibiting distinct layering characteristics. The misorientation angles of the α' phases are primarily distributed between 55° and 65° , which contributes to the anisotropy of the material.

References

1 Li W, Liu J, Wen S F *et al*. *Materials Characterization*[J], 2016, 113: 125

2 Gerd L, James C W. *Inkjet Based Fabrication for Additive Manufacturing*[M], Berlin: Springer, 2007: 15

3 Froyen L, Kruth J P, Van V J *et al*. *Journal of Materials Processing Technology*[J], 2004, 149(1–3): 616

4 Nie Jingjing, Ma Pingyi, Sun Jingli *et al*. *Rare Metal Materials and Engineering*[J], 2023, 52(6): 2126 (in Chinese)

5 Huang S H, Liu P, Hou L *et al*. *Journal of Advanced Manufacturing Technology*[J], 2013, 67: 1191

6 Tomus D, Tian Y, Rometsch P A *et al*. *Materials Science and Engineering A*[J], 2016, 667: 42

7 Liu Lun, Zhang Zhenjun, Yang Huajie *et al*. *Rare Metal Materials and Engineering*[J], 2021, 50(12): 4429 (in Chinese)

8 Li D, Chen J, Tan H *et al. Journal of Advanced Manufacturing Technology*[J], 2024, 53(9): 2503

9 Zhu Y Y, Tian X J, Li J *et al*. *Materials & Design*[J], 2015, 67: 538

10 Liu S Y, Shin Y C. *Materials & Design*[J], 2019, 164: 107552

11 Marco S, Yau Y T, Chris T. *Metallurgical and Materials Transactions A*[J], 2014, 45: 2863

12 Alphons A A. *Microstructure, Texture and Mechanical Property Evolution During Additive Manufacturing of Ti-6Al-4V Alloy for Aerospace Applications*[D]. Manchester: University of Manchester, 2012

13 Marco S. *Microstructure Evolution and Mechanical Properties of Selective Laser Melted Ti-6Al-4V*[D]. Leicestershire: Loughborough University, 2014

14 Evren Y, Jan D, Kruth J. *Rapid Prototyping Journal*[J], 2011, 17(5): 312

15 Banerjee D, Williams J C. *Acta Materialia*[J], 2013, 61(3): 844

16 Semiatin S L, Kinsel K T, Pilchak A L *et al. Metallurgical and Materials Transactions A*[J], 2013, 44(8): 3852

17 Semiatin S L, Bieler T R. *Metallurgical and Materials Transactions A*[J], 2001, 32(7): 1787

18 Soufiani A M, Karimzadeh F, Enayati M H. *Materials & Design*[J], 2012, 37: 152

19 Vrancken B, Thijs L, Kruth J P *et al. Journal of Alloys and Compounds*[J], 2012, 541: 177

20 Niendorf T, Leuders S, Riemer A *et al. Metallurgical and Materials Transactions B*[J], 2013, 44: 794

21 Thijs L, Sistiaga M L M, Wauthle R *et al. Acta Materialia*[J], 2013, 61(12): 4657

22 Vilaro T, Colin C, Bartout J D. *Metallurgical & Materials Transactions A*[J], 2011, 42(10): 3190

23 Yang J, Yu H, Wang Z *et al*. *Materials Characterization*[J], 2017, 127: 137

24 Song B, Dong S J, Zhang B C *et al. Materials & Design*[J], 2012, 35: 120

25 Han Jie. *Research on Anisotropy of Ti6Al4V Alloy Fabricated by Selective Laser Melting*[D]. Wuhan: Huazhong University of Science and Technology, 2016: 38 (in Chinese)

26 Yadroitsev I, Krakhmalev P, Yadroitsava I. *Journal of Alloys and Compounds*[J], 2014, 583: 404

27 Wang S C, Aindow M, Starink M J. *Acta Materialia*[J], 2003, 51(9): 2485

28 Ahmed T, Rack H J. *Materials Science and Engineering A*[J], 1998, 243(1–2): 206

29 Haize G, Robert J W, Diana A L *et al. Materials Science and Engineering A*[J], 2017, 685: 417

30 Filip R, Kubiak K, Ziaja W *et al. Journal of Materials Processing Technology*[J], 2003, 133: 84

31 Gey N, Humbert M, Gautier E *et al. Journal of Nuclear Materials*[J], 2004, 328(2–3): 137

32 Yang J J, Yu H C, Yang J *et al. Materials & Design*[J], 2016, 108: 308

选区激光熔化成形Ti-6Al-4V合金的力学各向异性

刘俊伟[1]，刘振亚[2]，范才河[1]，欧　玲[1]，何武强[1]，马五旦[1]

(1. 湖南工业大学 材料科学与工程学院，湖南 株洲 412007)

(2. 南昌航空大学 材料科学与工程学院，江西 南昌 330063)

摘　要：为了阐明选择性激光熔化成形Ti-6Al-4V合金的各向异性，研究了合金不同方向对应试样的压缩力学性能、显微硬度、显微组织和晶体取向。分析了力学性能的各向异性，并利用EBSD技术分析了不同晶粒类型和取向对不同尺度应力应变分布的影响。结果表明，室温下，当应变率为10^{-3} s^{-1}时，合金的抗压缩屈服强度和显微硬度随方向变化，呈现出各向异性。合金显微组织为柱状，沿沉积方向表现出等轴晶，其为内部致密六方（hcp）结构的α/α'马氏体结构。α'相择优取向近似<0001>。由于柱状晶长/宽比高，hcp织构弱，对称性差，导致了各向异性。

关键词：选区激光熔化；Ti-6Al-4V；各向异性；晶体取向

作者简介：刘俊伟，男，1981年生，博士，副教授，湖南工业大学材料与先进制造学院，湖南 株洲 412007，E-mail：liujw1981@126.com